

See discussions, stats, and author profiles for this publication at: <https://www.researchgate.net/publication/261405363>

Unraveling the Nanoscale Morphologies of Mesoporous Perovskite Solar Cells and Their Correlation to Device Performance

ARTICLE *in* NANO LETTERS · APRIL 2014

Impact Factor: 13.59 · DOI: 10.1021/nl5006838 · Source: PubMed

CITATIONS

18

READS

238

12 AUTHORS, INCLUDING:



Diana Nanova

Heidelberg University / TU Braunschweig

6 PUBLICATIONS 31 CITATIONS

[SEE PROFILE](#)



Martin Pfannmöller

University of Antwerp

13 PUBLICATIONS 151 CITATIONS

[SEE PROFILE](#)



Wilfried Hermes

BASF SE

120 PUBLICATIONS 1,497 CITATIONS

[SEE PROFILE](#)

Unraveling the Nanoscale Morphologies of Mesoporous Perovskite Solar Cells and Their Correlation to Device Performance

Diana Nanova,^{†,‡,§} Anne Katrin Kast,^{†,‡,||} Martin Pfannmöller,^{||} Christian Müller,^{†,‡,§} Lisa Veith,[⊥] Irene Wacker,[⊥] Michaela Agari,[¶] Wilfried Hermes,[¶] Peter Erk,[¶] Wolfgang Kowalsky,^{†,‡,§} Rasmus R. Schröder,^{‡,||,⊥,*} and Robert Lovrinčić*,^{†,‡}

[†]Institute for High-Frequency Technology, TU Braunschweig, 38106 Braunschweig, Germany

[‡]InnovationLab GmbH, 69115 Heidelberg, Germany

[§]Kirchhoff-Institute for Physics, Heidelberg University, 69117 Heidelberg, Germany

^{||}Cryo-EM, CellNetworks, BioQuant, Universitätsklinikum Heidelberg, 69120 Heidelberg, Germany

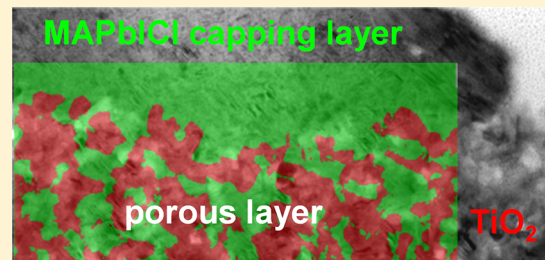
[⊥]Center for Advanced Materials, Heidelberg University, 69117 Heidelberg, Germany

[¶]BASF SE, 67056 Ludwigshafen, Germany

S Supporting Information

ABSTRACT: Hybrid solar cells based on organometal halide perovskite absorbers have recently emerged as promising class for cost- and energy-efficient photovoltaics. So far, unraveling the morphology of the different materials within the nanostructured absorber layer has not been accomplished. Here, we present the first visualization of the mesoporous absorber layer in a perovskite solar cell from analytical transmission electron microscopy studies. Material contrast is achieved by electron spectroscopic imaging. We found that infiltration of the hole transport material into the scaffold is low and inhomogeneous. Furthermore, our data suggest that the device performance is strongly affected by the morphology of the TiO₂ scaffold with a fine grained structure being disadvantageous.

KEYWORDS: *Perovskite solar cells, mesoporous solar cells, nanoscale morphology, analytical transmission electron microscopy, electron energy loss spectroscopy*



Organometal trihalide perovskites, such as methylammonium lead iodide¹ ($\text{CH}_3\text{NH}_3\text{PbI}_3$, herein MAPbI), are of great interest in material sciences as they combine excellent electronic properties with solution based processability. A great deal of work on this material class has been performed in the 1990s by Mitzi and co-workers.² Recently, organometal trihalide perovskites have emerged as promising absorber material for cost-efficient solar cells.^{3–5} Conversion efficiencies have increased from 3.8% in 2009⁶ to as to date above 15%^{7–9} at an unprecedented rate. All early reports utilized the absorber in combination with a mesoporous TiO₂ network as electron contact,^{6,10–13} in analogy to dye sensitized solar cells (DSSC). At a later stage, highly efficient cells with an electrically insulating alumina scaffold and in planar geometry, that is, without any scaffold, were demonstrated^{8,9,12,14,15} with the perovskite absorber prepared from chlorine-containing precursors (widely denoted $\text{CH}_3\text{NH}_3\text{PbI}_{3-x}\text{Cl}_x$, herein MAPbICl). The better performance of MAPbICl compared to MAPbI in planar cells is attributed to longer charge carrier diffusion lengths in excess of 1 μm .^{16–19} It is not clear which device architecture (planar or mesoporous) will find broader acceptance; planar cells are simpler in design and can be fabricated by both vapor-deposition and solution-processing, but the

mesoporous scaffold may improve film formation and surface coverage.⁴

In the case of perovskite solar cells with porous TiO₂ scaffold, an understanding of the relationship between atomic structure and nanoscale morphology of the absorber material versus device performance is of great importance for a rational design of the solar cells. The atomic structure of $\text{CH}_3\text{NH}_3\text{PbI}_3$ in TiO₂ has recently been investigated using pair distribution function analysis of high-quality X-ray diffraction data.²⁰ Several groups have used scanning electron microscopy (SEM) to study cross sections of such cells.^{7,13,21,22} Whereas this method is well suited for studying the thicknesses of individual layers, SEM does not provide the specific contrast necessary to unravel the nanoscale morphology within the mixed TiO₂/perovskite layer. Transmission electron microscopy (TEM) is in principle capable of imaging at very high resolution and thus providing direct atomic material information, but sample preparation is demanding and achieving material contrast is not always straightforward. So far there is only a single report on TEM

Received: February 22, 2014

Revised: March 31, 2014

Published: April 4, 2014



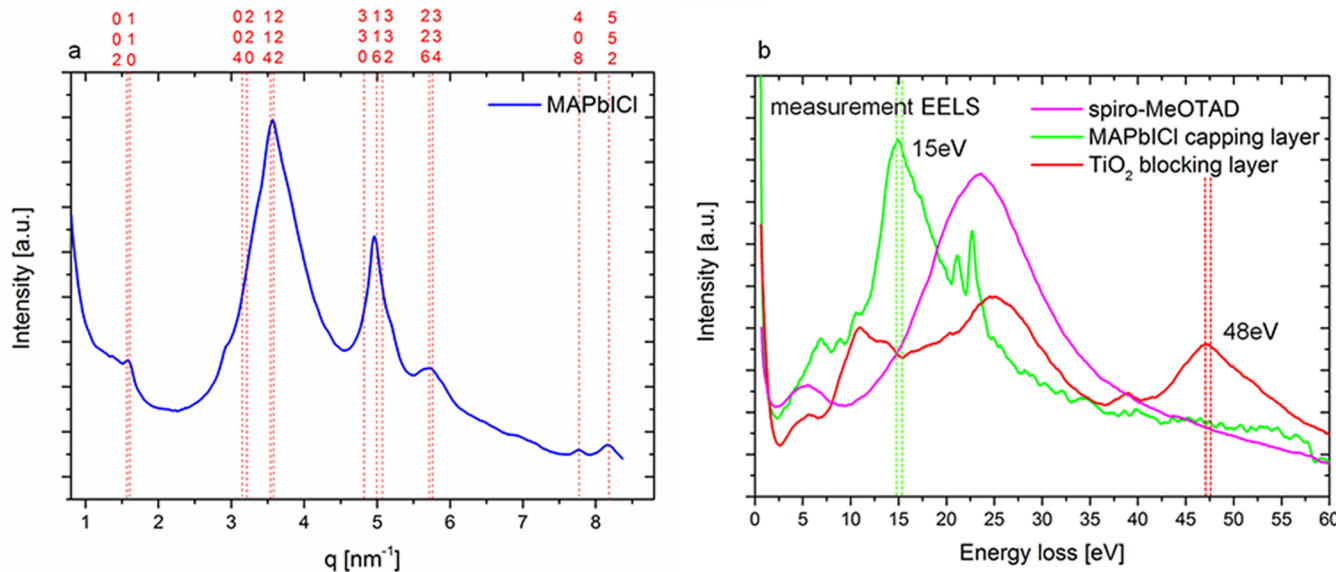


Figure 1. (a) Radial profile of a diffraction pattern measured on a MAPbClI TEM lamella. Vertical dotted lines mark expected peak positions for the corresponding lattice planes of the tetragonal MAPbI structure. (b) The EEL spectra of spiro-MeOTAD, MAPbClI, measured in the capping layer on top of the porous layer, and TiO₂, measured in the blocking layer. The MAPbClI shows pronounced features at 15, 21, and 23 eV, see text for details. The TiO₂ exhibits a broad excitation at around 48 eV that does not overlap with excitations in the MAPbClI.

measurements on cross sections of planar perovskite solar cells²³ and none for mesoporous cells.

We will show in this work that (i) material contrast between TiO₂ and MAPbClI even within the mesoporous layer can be obtained using a specialized statistical analysis of electron spectroscopic imaging (ESI) data, a method originally developed for polymer bulk-heterojunction solar cells,²⁴ (ii) infiltration of the hole transport material (HTM) into the TiO₂ scaffold is inhomogeneous over the device area but generally low, and that (iii) we can correlate our findings regarding morphology with device performance. Specifically, our data suggest that contrary to DSSCs a fine-grained structure of the porous TiO₂ is not a prerequisite for the solar cell efficiency. However, a high degree of connectivity within the TiO₂ is required for efficient electron transport and improved fill factors.

The samples were fabricated on FTO substrates coated with a 30 nm thick TiO₂ blocking layer. The TiO₂ porous layer was prepared by spin-coating a commercial TiO₂ paste (Dyesol 18NRT, Dyesol) diluted with ethanol on top and annealed at 450 °C for 30 min in a preheated convection oven. The perovskite was deposited by spin-coating from a N,N-dimethylformamide solution of methylammonium iodide and lead chloride (3:1 molar ratio) under ambient conditions and annealed for 30 min at 110 °C. After another 30 min of cool-down, the hole transport layer was spin-coated from a solution of 2,2',7,7'-tetrakis(*N,N*-di-*p*-methoxyphenylamine) 9,9'-spirobifluorene (spiro-MeOTAD), lithium bis-(trifluoromethanesulfonyl) imide (LiTFSI) and 4-*tert*-butylpyridine (tBP) in chlorobenzene. A gold electrode was evaporated on top of the device. The differences between the three devices are: device 1 was prepared with a lower concentration of spiro-MeOTAD (i.e., yielding a thinner layer) and optimized contents of LiTFSI and tBP. Devices 2 and 3 were annealed right after the MAPbClI deposition at different positions in the oven, significantly affecting the device performance; at the position of device 2, the temperature dropped by 10 K when the door was opened, whereas it dropped by 20 K at the

position of device 3. This small difference had a surprisingly strong effect on device efficiency; averaged efficiency was 5.5% for the position of device 2 and 2.9% for device 3 (averaged over 16 devices for each position). Before further treatment of the solar cells, the *I*–*V* characteristics and power conversion efficiencies were determined under AM 1.5 solar illumination. Cross sections of the samples were prepared by FIB milling with Ga⁺ ions in a Crossbeam Workstation AURIGA by Carl Zeiss Microscopy Oberkochen, Germany. Typically, a slice of the whole device stack including the substrate is milled as shown in the SEM image in the Supporting Information (Figure S1) and transferred by a micromanipulator onto an Omniprobe lift-out grid. Several small windows of the exposed cross section were polished down to approximately 100 nm in the low kV regime. The EELS (electron energy loss spectroscopy) and ESI measurements were realized with a Libra 200 MC KRONOS, Carl Zeiss Microscopy. The microscope features a monochromator combined with a higher-order aberration corrected in-column energy filter, which leads to a high energy resolution. The total electron dose applied for EELS was 7×10^3 electrons per nm² at an electron energy of 200 keV. ESI series were acquired from several windows of cross sections from three different devices. In this work, we show the analysis of the ESI series of one representative window for each device. The ESI images were recorded with a total electron dose of 10^6 electrons per nm², again at 200 keV primary electron energy. Images from 0 to 100 eV were acquired in steps of 1 eV with a 2 eV wide slit aperture. Before the statistical data analysis the images from the stack were aligned to minimize effects of sample drift. Subsequently, machine learning was used to distinguish between spectral classes in the images; because there is an image for every energy step, each spatial pixel can be expanded by a specific energy loss spectrum. As demonstrated by Pfannmöller et al.²⁴ locally linear embedding (LLE) can be applied to reduce data dimensionality. For this purpose, bright pixels in the characteristic monochromatic image of the different materials are chosen manually. In addition, this annotation is used to train a Random

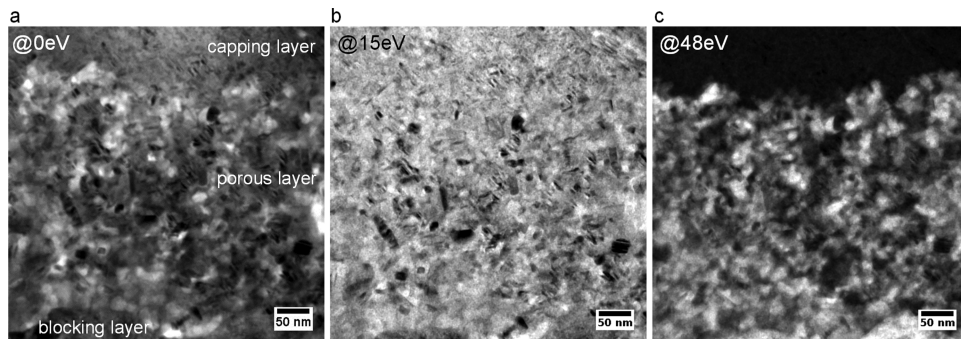


Figure 2. Low loss images of device cross section. (a) Zero-loss image shows several, almost continuous grades of intensities, which cannot be assigned to specific materials. (b,c) Monochromatic images from the ESI series exhibit differences in contrasts. As expected from the EELS measurements, at 15 eV (b) the perovskite capping layer along with features within the porous layer appear bright. The contrast of the perovskite capping layer is inverted at 48 eV (c). The blocking layer and round structures in the porous layer appear bright now and can be assigned to TiO_2 -rich areas. However, there is no uniform contrast inversion between the images.

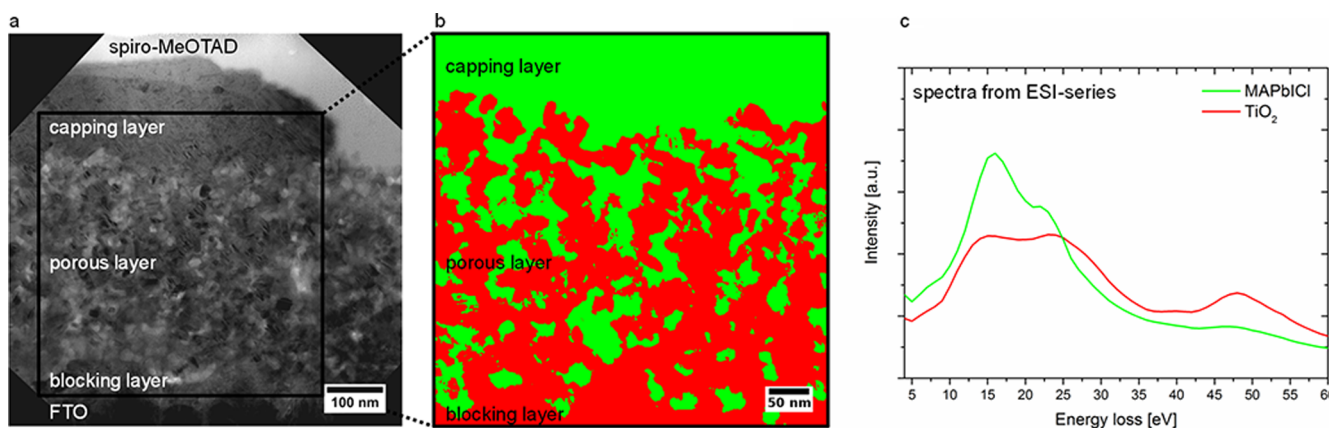


Figure 3. Classification of a typical cross section for device 1. (a) Zero-loss filtered image of a typical analyzed area. The multivariate statistical analysis (MSA) was carried out on the detail indicated by the rectangle. (b) Classification of (red) TiO_2 - and (green) perovskite-rich areas after statistical analysis of the ESI series. The TiO_2 shows a highly connected network. The pores of 10–80 nm are filled with perovskite. (c) The spectra of the perovskite and the TiO_2 extracted from the ESI series exhibit features at 15 and 48 eV, which is in good agreement with the EEL spectra shown in Figure 1. Because of the lower energy resolution of ESI spectral features are not as well resolved as in the EEL spectra.

Forest classifier, which is applied for the automated assignment of the pixels. Thus, spectra exhibiting the same features are combined to one class.

To exclude that the MAPbICl was altered during the preparation of the cross sections by focused ion beam (FIB) milling we first performed electron diffraction measurements. We compared the results with known values^{1,25} for MAPbI, as the peak positions in X-ray diffraction for MAPbI and MAPbICl are in excellent agreement⁸ and the question if and how the Cl is incorporated into the crystal structure is to date an open one.

Figure 1a shows the radial profile of a diffraction pattern measured on a MAPbICl TEM lamella. These diffraction patterns are recorded usually from areas containing a small number of single crystals, that is, their intensity distribution is neither identical to the typical powder diffraction nor to oriented single crystals. The vertical lines mark the theoretical peak positions for the corresponding lattice planes of the tetragonal MAPbI structure.²⁵ Clearly all observed peak positions can be explained by the MAPbI structure. Figure 1b presents the EEL spectra of pure MAPbICl, TiO_2 , and spiro-MeOTAD in the low loss regime. The most prominent features of the EEL spectrum of the MAPbICl are a broad peak at 15 eV and two sharp peaks between 20 and 25 eV. The two sharp peaks can be assigned to localized core excitations arising from

the 5d core levels of the Pb^{2+} ions.²⁶ The broad structure at 15 eV, judged by its shape and energetic position, is most probably related to an excitation of the valence band plasmon of the MAPbICl. We note that to the best of our knowledge this is the first published EEL spectrum of MAPbICl in the low loss regime. The spectrum of the blocking layer corresponds very well with published EELS data for TiO_2 .^{27,28} Most notably, the titanium $M_{2,3}$ edge at 48 eV, representing transitions from electrons in the titanium $3p_{1/2}$ and $3p_{3/2}$ core-shells to empty energy states in the conduction band,²⁷ does not overlap with excitations in the MAPbICl. The spiro-MeOTAD spectrum is dominated by its plasmon peak at 24 eV. In the following, we use the TiO_2 peak at 48 eV and the MAPbICl peak at 15 eV to distinguish the two materials in a mesoporous perovskite solar cell by monochromatic imaging at these two loss energies.

We use the cross section of a well-performing solar cell (device 1, power conversion efficiency ~9%) to demonstrate our analytical TEM approach. A zero-loss filtered image of this cross section is shown in Figure 2a with the TiO_2 blocking layer at the bottom, the mesoporous $\text{TiO}_2/\text{MAPbICl}$ in the middle, and a MAPbICl capping layer on top. Such perovskite capping layers are found frequently, and it is believed they form after maximum pore filling is reached.¹² For this type of image, the inelastically scattered electrons are filtered out and only the

elastically scattered electrons contribute to the image signal. We observe several, almost continuous grades of intensities. However, the zero-loss image does show a phase difference between the textured porous layer and the perovskite capping layer. Inelastic images for 15 and 48 eV energy loss are presented in Figure 2b,c, respectively. At 15 eV, the image appears brighter and the transition between the porous layer and the capping layer is hardly visible, which we explain with the non-negligible intensity of the TiO_2 loss spectrum at this energy (see Figure 1b). At 48 eV, we observe a contrast inversion for the perovskite capping layer and in parts of the TiO_2 blocking layer. It is not possible to fully distinguish between the perovskite and the TiO_2 within the porous layer as we do not observe an obvious uniform contrast inversion for this area between the images at 15 and 48 eV. Thus, the inelastic images in Figure 2b,c provide material contrast but are not sufficient for a complete classification within the mesoporous structure. To achieve such a specific classification, we turn to the analysis of the entire ESI stack from 0 to 100 eV. Applying multivariate statistical analysis for the categorization of each pixel from the stack and classification of the associated spectra results then in a significant two-class separation of the layers.²⁴

Figure 3 shows a representative example of an ESI series analysis. Panel a is the cross section of device 1 at zero energy loss. The black square marks the area chosen for the ESI analysis. The two-class segmentation of the area is shown in Figure 3b. MAPbI_{Cl} rich domains are green; TiO_2 rich domains are red. The typical size of domains in the material classification is smaller than the thickness of the lamella. Thus, a certain overlap of materials in the TEM projection images is likely. However, this does not prohibit a first comparison of relative material distribution, as domains are classified according to a higher or lower contribution of the materials and not according to pure phases.²⁴ The TiO_2 shows a highly connected network and continuous paths from the blocking layer to the top. The pore size varies from 10 to 80 nm. The perovskite capping layer is penetrating into the porous layer. We did not find any indication for HTM under the capping layer. The ESI spectra obtained from the classification of the pixels are shown in Figure 3c. The TiO_2 spectrum is in excellent agreement with the EELS data from the blocking layer (compare Figure 1b). Even the small feature at 39 eV loss is reproduced. The MAPbI_{Cl} spectrum is still dominated by the plasmon resonance at 15 eV. Because of the lower energy resolution of the ESI data compared to EELS, the two peaks corresponding to the 5d core levels appear now as one shoulder at 23 eV. The small bump at 48 eV points to a slight cross-talk by the statistical assignment between TiO_2 and MAPbI_{Cl}.

Whether the HTM partially infiltrates the porous layer, or the pores are completely filled with MAPbI_{Cl}, and how this is affected by a perovskite capping layer relates to the fundamental question of what kind of solar cell we are dealing with: DSSC, extremely thin absorber, or p-i-n devices. Figure 4 shows a series of ESI spectra at different depths for positions with and without capping layer. Below the capping layer, the data are well described as superpositions of the TiO_2 and MAPbI_{Cl} loss spectra (see Figure S2 in Supporting Information), just as expected from the classification shown in Figure 3. Without the capping layer, the HTM infiltrates roughly the first 100 nm of the TiO_2 scaffold, evident from the dominance of the peak at 24 eV. At a depth of 150 nm within the porous layer, the spectrum can only be described accurately

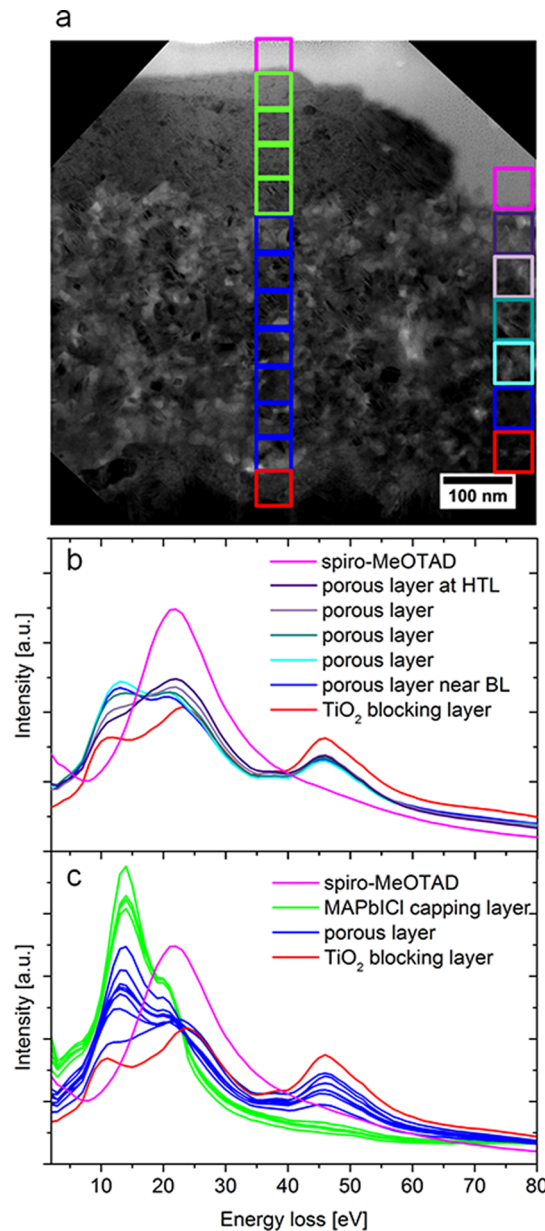


Figure 4. Infiltration of HTM into the scaffold as visualized by ESI spectra. (a) The same cross section as in Figure 2 was used to extract spectra at different depths in areas with and without MAPbI_{Cl} capping layer (spots marked by colored squares). (b) Without the capping layer, the HTM infiltrates the first ~100 nm of the TiO_2 scaffold. (c) The spectra from under the capping layer indicate no HTM infiltration.

with a HTM content of no more than 5% (see Figure S2 in Supporting Information). This is in contrast to publications on mesoporous perovskite solar cells that assume a thin coating of the TiO_2 with MAPbI(Cl) and the hole transporter in the pores for optimized devices.^{12,13,29} We conclude that in agreement with recent findings¹⁸ MAPbI_{Cl} perovskite solar cells are best viewed as p-i-n type solar cells, even when prepared with a porous TiO_2 electron transport layer.

In order to highlight the relationship between device performance and morphology of the mesoporous layer, we investigated two additional solar cells (devices 2 and 3) that were prepared in parallel with slightly deviating annealing procedures as explained above and consequently performed

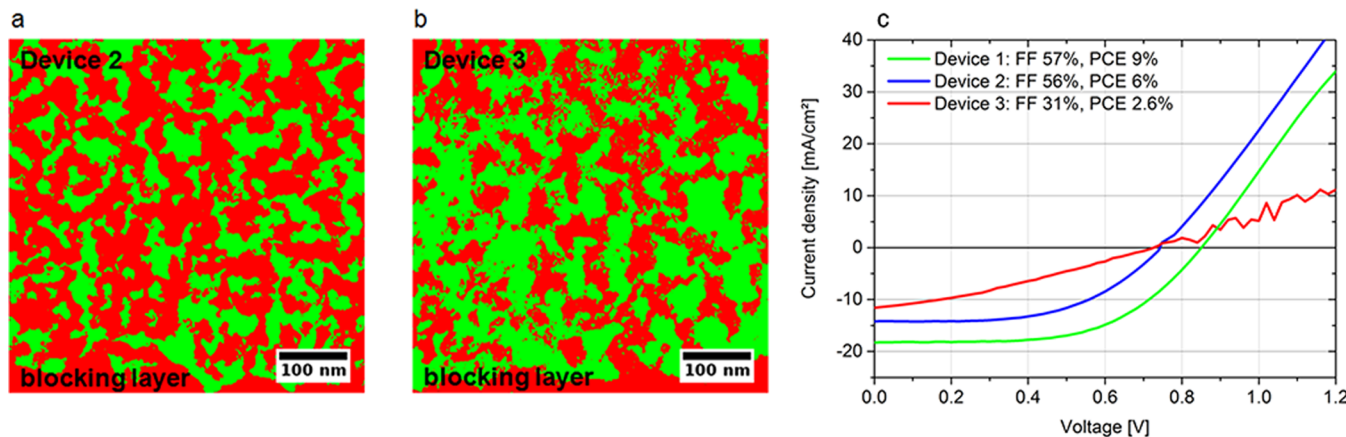


Figure 5. Correlation between morphology and device characteristics. (a) Device 2 exhibits a compact and well-connected TiO_2 network. (b) The TiO_2 in device 3 is much finer grained structure (very small and unconnected red domains). (c) I - V characteristics of the devices. The higher fill factors of devices 1 and 2 can be correlated to the well-connected TiO_2 network and hence better electron transport properties.

distinctively different (efficiencies of 5.8 and 2.6% for devices 2 and 3, respectively). Figure 5a,b shows the cross sections of devices 2 and 3, respectively, after materials classification. In Figure 5c, we plot the I (V) curves for all three investigated solar cells (see Table S1 in Supporting Information for full device parameters).

Evidently, the lowest performing device 3 with a very low fill factor of 31% exhibits a much finer grained TiO_2 structure compared to device 2. Because the TiO_2 scaffold was prepared in the same way for both devices, we assume that the different heating conditions of the two cells led to a different crystallization of the perovskite affecting also the structure of the scaffold. The exact mechanism is unclear and detailed understanding would request further studies that are beyond the scope of this work. While we cannot rule out other additional reasons for the difference in efficiency, we rationalize, based on the correlation between morphology and device performance, that the observed fine grained TiO_2 structure does not provide the high electron transport capabilities needed for high-efficiency cells, leading to charge carrier recombination and ultimately to low fill factors.

The calculated power density spectra (see Figure S3 in Supporting Information for data) show higher intensities for device 3 at structure sizes smaller than 30 nm, confirming the visual impression. Again, this is in contrast to DSSCs where a high TiO_2 surface area is of uttermost importance for good cell performance. Complementary, the fill factor is not negatively affected by a more slender structuring of the MAPbI_3 due to its excellent electronic quality.

In summary, we showed that analytical TEM studies on cross sections are a very powerful tool to investigate the morphology of mesostructured perovskite solar cells. TiO_2 and MAPbI_3 can be clearly distinguished on the nanoscale by their EEL spectra. Our data suggest that HTM infiltration in optimized mesoporous TiO_2 / MAPbI_3 cells is low and high TiO_2 surface area does not improve device performance, lending additional credence to the notion that mesoporous TiO_2 / MAPbI_3 cells can be viewed as p-i-n type. We believe these findings will promote the detailed understanding of the working principle of mesostructured perovskite solar cells and can be helpful for a further device optimization.

■ ASSOCIATED CONTENT

■ Supporting Information

Details on TEM-lamella preparation; detailed analysis of the porous layer beneath HTM; power density spectra of the segmentation of devices 2 and 3; device characteristics of devices 1, 2, and 3. This material is available free of charge via the Internet at <http://pubs.acs.org>.

■ AUTHOR INFORMATION

Corresponding Authors

*E-mail: rasmus.schroeder@bioquant.uni-heidelberg.de.
*E-mail: r.lovrincic@tu-braunschweig.de.

Author Contributions

D.N and A.K.K. contributed equally to this work.

Device fabrication, optimization, and characterization: M.A., C.M., W.H., and P.E. TEM sample preparation: D.N., L.V., and I.W. TEM measurements and data analysis: D.N., A.K.K., and M.P. Data interpretation and manuscript writing: D.N., A.K.K., M.A., W.H., P.E., W.K., R.R. S., and R. L.

Notes

The authors declare no competing financial interest.

■ ACKNOWLEDGMENTS

We acknowledge financial support from the German Ministry of Education and Research (FKZ 13N10794, 13N12279, and 03EK3505J,L,K).

■ REFERENCES

- (1) Weber, D. Z. *Naturforsch., B: Chem. Sci.* **1978**, *33*, 1443.
- (2) Mitzi, D. B. In *Progress in Inorganic Chemistry*; Karlin, K. D., Ed.; John Wiley & Sons, Inc.: New York, 2007; pp 1–121.
- (3) Hodes, G. *Science* **2013**, *342*, 317–318.
- (4) Snaith, H. J. *J. Phys. Chem. Lett.* **2013**, *3623–3630*.
- (5) Park, N.-G. *J. Phys. Chem. Lett.* **2013**, *4*, 2423–2429.
- (6) Kojima, A.; Teshima, K.; Shirai, Y.; Miyasaka, T. *J. Am. Chem. Soc.* **2009**, *131*, 6050–6051.
- (7) Burschka, J.; Pellet, N.; Moon, S.-J.; Humphry-Baker, R.; Gao, P.; Nazeeruddin, M. K.; Grätzel, M. *Nature* **2013**, *499*, 316–319.
- (8) Liu, M.; Johnston, M. B.; Snaith, H. J. *Nature* **2013**, *501*, 395–398.
- (9) Liu, D.; Kelly, T. L. *Nat. Photonics* **2014**, *8*, 133–138.
- (10) Im, J.-H.; Lee, C.-R.; Lee, J.-W.; Park, S.-W.; Park, N.-G. *Nanoscale* **2011**, *3*, 4088–4093.

- (11) Etgar, L.; Gao, P.; Xue, Z.; Peng, Q.; Chandiran, A. K.; Liu, B.; Nazeeruddin, M. K.; Grätzel, M. *J. Am. Chem. Soc.* **2012**, *134*, 17396–17399.
- (12) Lee, M. M.; Teuscher, J.; Miyasaka, T.; Murakami, T. N.; Snaith, H. J. *Science* **2012**, *338*, 643–647.
- (13) Kim, H.-S.; Lee, C.-R.; Im, J.-H.; Lee, K.-B.; Moehl, T.; Marchioro, A.; Moon, S.-J.; Humphrey-Baker, R.; Yum, J.-H.; Moser, J. E.; Grätzel, M.; Park, N.-G. *Sci. Rep.* **2012**, *2*, 591.
- (14) Chen, Q.; Zhou, H.; Hong, Z.; Luo, S.; Duan, H.-S.; Wang, H.-H.; Liu, Y.; Li, G.; Yang, Y. *J. Am. Chem. Soc.* **2013**, *135*, 8484–8487.
- (15) Ball, J. M.; Lee, M. M.; Hey, A.; Snaith, H. J. *Energy Environ. Sci.* **2013**, *6*, 1739–1743.
- (16) Stranks, S. D.; Eperon, G. E.; Grancini, G.; Menelaou, C.; Alcocer, M. J. P.; Leijtens, T.; Herz, L. M.; Petrozza, A.; Snaith, H. J. *Science* **2013**, *342*, 341–344.
- (17) Xing, G.; Mathews, N.; Sun, S.; Lim, S. S.; Lam, Y. M.; Grätzel, M.; Mhaisalkar, S.; Sum, T. C. *Science* **2013**, *342*, 344–347.
- (18) Edri, E.; Kirmayer, S.; Henning, A.; Mukhopadhyay, S.; Gartsman, K.; Rosenvaks, Y.; Hodes, G.; Cahen, D. *Nano Lett.* **2014**, DOI: 10.1021/nl404454h.
- (19) Wehrenfennig, C.; Eperon, G. E.; Johnston, M. B.; Snaith, H. J.; Herz, L. M. *Adv. Mater.* **2013**, *26*, 1584–1589.
- (20) Choi, J. J.; Yang, X.; Norman, Z. M.; Billinge, S. J. L.; Owen, J. S. *Nano Lett.* **2014**, *14*, 127–133.
- (21) Noh, J. H.; Im, S. H.; Heo, J. H.; Mandal, T. N.; Seok, S. I. *Nano Lett.* **2013**, *13*, 1764–1769.
- (22) Zhang, W.; Saliba, M.; Stranks, S. D.; Sun, Y.; Shi, X.; Wiesner, U.; Snaith, H. J. *Nano Lett.* **2013**, *13*, 4505–4510.
- (23) Sun, S.; Salim, T.; Mathews, N.; Duchamp, M.; Boothroyd, C.; Xing, G.; Sum, T. C.; Lam, Y. M. *Energy Environ. Sci.* **2013**, *7*, 399–407.
- (24) Pfannmöller, M.; Flügge, H.; Benner, G.; Wacker, I.; Sommer, C.; Hanselmann, M.; Schmale, S.; Schmidt, H.; Hamprecht, F. A.; Rabe, T.; Kowalsky, W.; Schröder, R. R. *Nano Lett.* **2011**, *11*, 3099–3107.
- (25) Baikie, T.; Fang, Y.; Kadro, J. M.; Schreyer, M.; Wei, F.; Mhaisalkar, S. G.; Graetzel, M.; White, T. J. *J. Mater. Chem. A* **2013**, *1*, 5628–5641.
- (26) Scrocco, M. *J. Electron Spectrosc. Relat. Phenom.* **1989**, *48*, 363–374.
- (27) Bosman, M.; Watanabe, M.; Alexander, D. T. L.; Keast, V. J. *Ultramicroscopy* **2006**, *106*, 1024–1032.
- (28) Ahn, C. C.; Krivanek, O. L. *EELS Atlas: a reference guide of electron energy loss spectra covering all stable elements*; ASU HREM Facility & Gatan Inc.: Warrendale, PA, 1983.
- (29) Abrusci, A.; Stranks, S. D.; Docampo, P.; Yip, H.-L.; Jen, A. K.-Y.; Snaith, H. J. *Nano Lett.* **2013**, *13*, 3124–3128.